Hydrogen-interstitial CuWO$_4$ nanomesh: A single-component full spectrum-active photocatalyst for hydrogen evolution

Zhaoyong Lin, Weijia Li, Guowei Yang[*]

State Key Laboratory of Optoelectronic Materials and Technologies, Nanotechnology Research Center, School of Materials Science & Engineering, Sun Yat-sen University, Guangzhou 510275, Guangdong, PR China

ARTICLE INFO

ABSTRACT

It is of practical and theoretical significance to realize full spectrum-active photocatalytic hydrogen (H$_2$) evolution using a single-component photocatalyst. The bottleneck is the utilization of near infrared (NIR) light with 52% of the energy in solar spectrum due to the mismatch between its low single photon energy and the large bandgaps of many photocatalysts. In fact, except for the intrinsic inter-band transition, charge-transfer transition is another strategy to produce hot electrons as a result of light excitation. Herein, charge-transfer transition is achieved in hydrogen-interstitial CuWO$_4$ nanomesh (H-CuWO$_4$) by introducing low-valence Cu$^+$ and W^{5+}. The resulting polaron absorption produces abundant free electrons upon NIR irradiation. Meanwhile, the intrinsic inter-band transition supplies more electrons upon ultraviolet and visible (UV and Vis) irradiations. The mesh structure induced by the self-assembled orientated attachment facilitates the electron transport in the photo-catalytic process. Further, the lattice stress resulting from the H intercalation raises the conduction band (CB) above the H$^+$/H$_2$ potential level. CuWO$_4$, incapable of realizing photocatalytic H$_2$ evolution, is therefore activated to be a single-component full spectrum-active photocatalyst based on the dual-channel mechanism without any assistance of cocatalysts. It exhibits an excellent H$_2$ evolution rate and high stability. This advance may have great potential in the future environmental and energy engineering applications.

1. Introduction

Photocatalytic hydrogen (H$_2$) evolution is a promising approach to supplying clean fuels from abundant solar energy [1,2]. Realization of full spectrum-active photocatalysis is severely constrained by the utilization of near infrared (NIR) irradiation, which occupies 52% of the energy in solar spectrum [3]. This predicament is on account of the poor NIR irradiation harvesting capacities of many photocatalysts resulting from the mismatch between their wide bandgaps and the low single NIR photon energy [4]. So far, several kinds of NIR irradiation-responsive materials have been developed, *e.g.*, up-conversion, narrow-bandgap and plasmonic materials [5–11]. It is with regret that they are unable to act as single-component photocatalysts due to their intense carrier recombination [12].

As a matter of fact, metal-to-metal charge transfer (MMCT) is another effective strategy to produce hot electrons upon NIR irradiation [13]. It is usually achieved by self-doping with a low-valence element. Generally, this structural modification perturbs the lattice symmetry and produces an internal electric field. Polaron absorption accompanied by MMCT therefore takes place upon NIR irradiation [14]. The

generated electrons and holes are separated on two spatial sites, *i.e.*, two neighboring nonequivalent metal atoms. It endows the MMCT-based materials with the potential as NIR irradiation-active photocatalysts. As a consequence, NIR irradiation-driven photocatalytic organic contaminants degradation has been realized in many MMCT-based materials, *e.g.*, Cu$_2$(OH)PO$_4$ (Cu$^+$/Cu^{2+}/Cu^{3+}), Co$_{2.67}$S$_4$ (Co^{2+}/Co^{3+}) and W$_{18}$O$_{49}$ (W^{5+}/W^{6+}) [15–17]. Nevertheless, it is still rare for this MMCT effect to be applied to photocatalytic H$_2$ evolution due to the more rigorous requirement of suitable electronic structures.

Copper tungstate (CuWO$_4$) is a well-known robust photocatalyst [18], but it is NIR irradiation-inactive and unable to realize H$_2$ evolution due to its lower CB location with respect to the H$^+$/H$_2$ potential level [19]. It is considered that NIR irradiation absorption may be gained by CuWO$_4$ since MMCT frequently emerges in the materials containing Cu and/or W elements. Moreover, as one of the poly-xometalates, its electronic structure is modifiable and tunable on account of the prominent structure-directing effect [20,21]. The structural modification, *i.e.*, self-doping with low valence Cu and/or W elements may activate CuWO$_4$ to act as full spectrum-active photocatalyst for H$_2$ evolution.

In this contribution, the hydrogen-interstitial $CuWO_4$ nanomesh (H-$CuWO_4$) was prepared using the technology of laser ablation in liquid (LAL) [22,23]. Both Cu^{2+} and W^{6+} were partially reduced to low-valence Cu^+ and W^{5+} because of the intercalation of electron-donating H atoms. MMCT endows the H-$CuWO_4$ nanomesh with abundant hot electrons upon NIR irradiation. The stress resulting from the varying octahedral ligand field leads to the lifting of Fermi level and conduction band (CB), making CB be above the H^+/H_2 level [24]. Therefore, the single-component H-$CuWO_4$ nanomesh becomes thermodynamically capable of photocatalytic H_2 evolution through water splitting. The reactions can be driven by not only ultraviolet and visible (UV and Vis) irradiations, but also NIR light. Further, the mesh structure induced by the self-assembled orientated attachment kinetically facilitates the electron transport. The photocatalyst exhibits an excellent photocatalytic rate and high stability based on a dual-channel mechanism. These findings shed new light on the activation of the inactive photocatalysts and the design of single-component full spectrum-active photocatalysts for clean fuels production.

2. Experimental section

2.1. Synthesis of H-CuWO₄ nanomesh

H-$CuWO_4$ nanomesh was prepared by LAL. Typically, 20.0-mg $CuWO_4$ powders (Alfa Aesar, 99%) and 12-mL ethanol were added into an 18-mL glass bottle. The powders were dispersed evenly by ultrasonic oscillation for 20 min. After that, the suspension was fixed on a magnetic stirrer for gently stirring. A second harmonic produced by a Q-switched Nd:YAG laser device was focused by a lens (100 mm) into the suspension. The laser wavelength, pulsed width, repeating frequency and pulse energy are respectively 532 nm, 10 ns, 10 Hz and 200 mJ. The LAL process was lasted for 2 h till no obvious powders were suspending. For tailoring the H intercalation degree, the laser pulse energy was adjusted in a large range. The products were labeled as H-$CuWO_4$-x while x represented the laser pulse energy (respectively 100, 150, 200, 250, 300 mJ). For comparison, the $CuWO_4$ powders were also ablated in de-ionized water with a laser pulse energy of 200 mJ. The product was labeled as $CuWO_4$-200. After the LAL process, the samples were centrifuged and washed with de-ionized water and ethanol. Finally, they were dried at 60 °C for the following characterizations and measurements.

2.2. Materials characterization

The morphology of the samples was observed by a thermal FE environment scanning electron microscope (SEM, Quanta 400, FEI Company) and an FEI Tecnai G2 F30 transmission electron microscope (TEM). The structures of the samples were characterized according to the X-ray diffraction (XRD) patterns using an X-ray diffractometer (D/MAX-2200, Rigaku). Fourier transform infrared (FTIR) spectra were recorded on a FTIR spectrometer (Nicolet6700, Thermo Scientific, USA). Raman vibrational modes were detected by an inVia Raman microscope (Renishaw, England) with an Ar laser (514.5 nm). An Via Reflex Microscope (Renishaw, England) with a He-Cd laser (325 nm) was used for photoluminescence (PL) measurements. X-ray photoelectron spectroscopy (XPS) and valence band (VB) XPS spectra were obtained on a XPS Scanning Microprobe spectrometer (Escalab 250, Thermo-VG Scientific, England, Al Kα). A UV–vis-NIR spectrophotometer (Lambda950, PerkinElmer Company) was used to record the diffuse reflectance absorbance spectra using $BaSO_4$ as a reference. Mott-Schottky plots were recorded in a three-electrode electrochemical cell at a frequency of 1 kHz in the dark. The measurements were performed in 0.5-M Na_2SO_4 electrolyte with a Pt counter electrode and saturated Ag/AgCl electrode. The gravimetric copper and tungsten were measured by inductive coupled plasma-atomic emission spectrometry (ICP-AES, IRIS(HR)). A gas chromatography-mass spectrometer (GC–MS) was used for GC–MS analysis. Thermogravimetry (TG) curves were obtained on a NETZSCH TG 209 F3 thermal analyzer.

2.3. Photocatalytic H₂ evolution

Photocatalytic H_2 evolution activity was estimated at 4 °C in a top-irradiation-type Pyrex glass cell connected to a closed gas-circulation system. 20.0-mg photocatalyst was added into the glass cell filled with 100-mL 20 vol.% ethanol aqueous solution. After a 30-min degassing pretreatment, the suspension was irradiated by a Xe lamp for 5 h. An AM 1.5 filter (CEAuLight, China) was fixed at the light outlet to simulate the solar irradiation (100.00 mW cm^{-2}). Three band-pass filters were added respectively to extract ultraviolet (UV, 200–420 nm, 8.42 mW cm^{-2}), visible (Vis, 420–760 nm, 42.74 mW cm^{-2}) and near infrared (NIR, 760–2100 nm, 48.36 mW cm^{-2}) irradiations from the simulated solar light. In addition, before going through the AM 1.5 filter, the light from a Xe lamp was reflected by a UV–vis reflector to extract UV and Vis irradiations (UV&Vis, 200–760 nm, 53.44 mW cm^{-2}) together from the simulated solar light. Single-wavelength activity in the NIR region was carried out with another band pass filter at the light outlet (780 ± 15, 850 ± 15 nm). Further, H-$CuWO_4$-200 photocatalyst irradiated by AM 1.5 was collected by centrifugation after the photocatalytic reactions. It was reused for four times to examine its photostability.

3. Results and discussion

3.1. Morphology and structure of H-CuWO₄ nanomesh

The H-$CuWO_4$ nanomesh was prepared by ablating bulk $CuWO_4$ powders (b-$CuWO_4$) by a nanosecond pulsed laser (200 mJ/pulse) in ethanol involving a technology called laser ablation in liquid (LAL). Microscaled irregular b-$CuWO_4$ (Fig. S1) has evolved into a mesh (Fig. 1a) woven by a series of fibers with various lengths consisting of irregular nanoparticles (Fig. 1b). HRTEM image in Fig. 1c presents a typical interplanar spacing of 0.2509 nm, which can also be found in b-$CuWO_4$. The nanomesh preserves the crystalline phase of b-$CuWO_4$ ($CuWO_4·2H_2O$, JCPDS 33-0503), as indicated in the XRD patterns in Fig. 1d. The diffraction peaks become broader due to the reduction of crystalline size. In addition, the three small peaks marked by "*" can be ascribed to the formation of $Cu_2WO_4(OH)_2$ phase (JCPDS 34-1297). It reveals the introduction of a small amount of OH species into the Cu_2WO_4 lattice. The slight left shift of the diffraction peaks demonstrates this deduction due to the resulting lattice expansion [25].

The atomic vibration of b-$CuWO_4$ and H-$CuWO_4$ were studied by FTIR spectroscopy (Fig. 1e). It is seen that the bands in the range from 400 to 900 cm^{-1} appear strongly. They should be attributed to the metal−O stretching vibrations [26]. In detail, as shown in the inset, they can be split into three kinds of vibration modes: Cu−O (400–530 cm^{-1}), W−O (530–750 cm^{-1}) and Cu−O−W (750–900 cm^{-1}). These modes are weaker and blurrier for H-$CuWO_4$ because of the lattice distortion. The peaks around 1627 and 3402 cm^{-1} refer to OH bending and stretching vibration modes due to the lattice water [27]. The most notable is that the appearance of the band at 1386 cm^{-1} [28]. It corresponds to the O−H bonds (a H atom bound to an O atom) named as H-related defects [29]. It means that H atoms are interstitial in the $CuWO_4$ lattice and bound to neighboring O anions to form metal−OH species. It should be the reason for the appearance of $Cu_2WO_4(OH)_2$ phase in the XRD patterns. These H-related defects are believed to be more thermally stable than lattice water molecules. Thermogravimetric (TG) measurements (Fig. 1f) were conducted to monitor the thermo-stability. The weight loss (10%) in the range of 60–150 °C should be associated with the evaporation of lattice water molecules in $CuWO_4·2H_2O$. The additional weight loss of 3% up to 350 °C should be due to the removal of lattice OH, that is, the H-related defects [30].
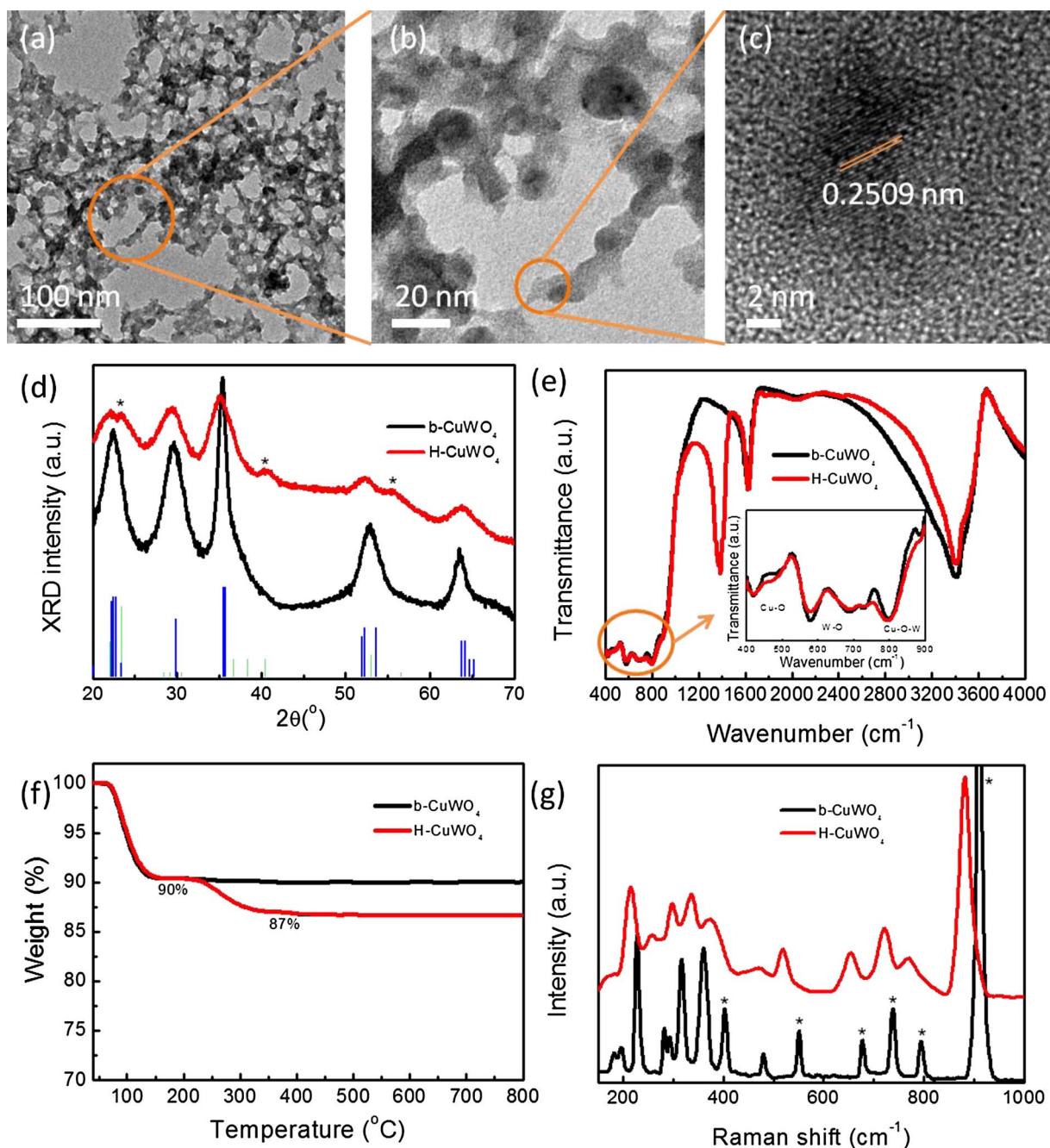
Fig. 1. (a) Low-magnification TEM, (b) high-magnification TEM, (c) HRTEM images of H-CuWO$_4$. (d) XRD patterns (standard XRD patterns of CuWO$_4$·2H$_2$O and Cu$_2$WO$_4$(OH)$_2$ are respectively shown by blue and green lines), (e) FTIR spectra, (f) TG curves and (g) Raman spectra of b-CuWO$_4$ and H-CuWO$_4$. (For interpretation of the references to colour in this figure legend, the reader is referred to the web version of this article.)

The Raman pattern of b-CuWO$_4$ is in good agreement with the standard one. According to the group theory, 18 Raman modes are expected [31]. As shown in Fig. 1g, 14 active modes are recognizable. The six modes marked by "*"correspond to the internal modes, which imply the normal motion of O atoms against W inside the [WO$_6$] octahedras. The others are external modes suggesting the movement of [WO$_6$] octahedral against Cu atoms [32]. The Raman modes of H-CuWO$_4$ are broader, indicating the slight structural disorder. Further, they show an obvious left shift. It should be on account of the lattice expansion, identical to the XRD results. According to Hardcastle and Wachs [33], the total valence of W (χ, given in valence units, v.u.) can be estimated based on the six internal W-O mode frequencies (ω_i, given in cm^{-1}):

$$\chi = \sum_{i=1}^{6} [0.27613 \ \ln(25823/\omega_i)]^{-6}$$

(1)

The total valences of W of b-CuWO$_4$ and H-CuWO$_4$ can be respectively estimated as 6.09 and 5.72. It is apparent that W elements of H-CuWO$_4$ are partially reduced.

XPS analysis was carried out to examine the chemical compositions and element valence states of the samples. As shown in Fig. S2, except for C element from the surroundings and Si element from the substrate, only Cu, W and O elements can be detected in both samples. The ratios of Cu:W in b-CuWO$_4$ and H-CuWO$_4$ are respectively 1.51 and 1.53, larger than the stoichiometry of CuWO$_4$. It may be because CuWO$_4$ is usually Cu-terminal. ICP measurements were further carried out. The ratios are respectively determined as 0.97 and 0.95, approaching the
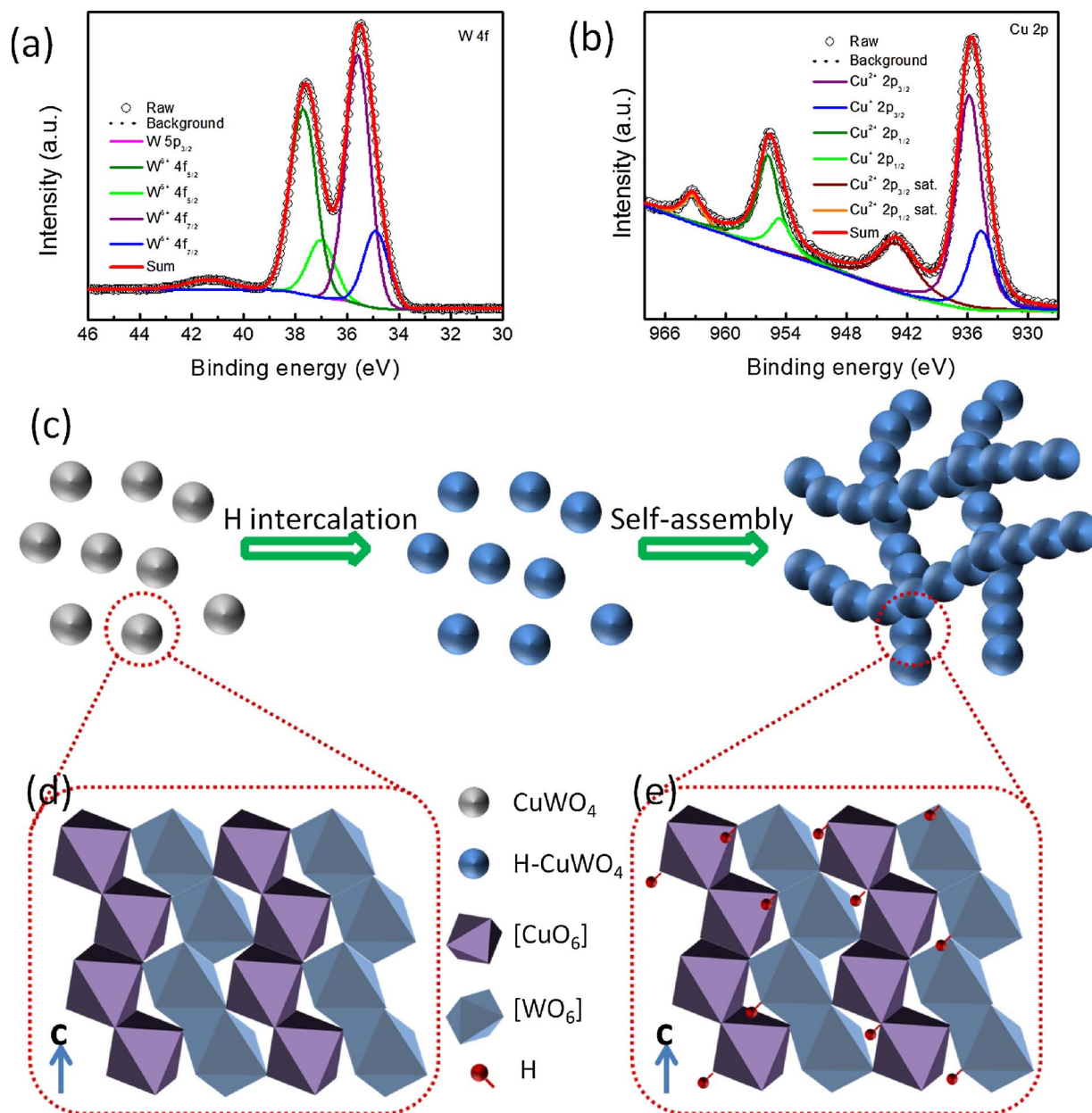
Fig. 2. (a) W 4f and (b) Cu 2p XPS spectra of H-CuWO$_4$. (c) Schematic illustration of the LAL process including H interstitial and self-assembly. (d-e) Schematic illustration of the crystal structures of (d) b-CuWO$_4$ and (e) H-CuWO$_4$.

stoichiometry of CuWO$_4$. It reveals that neither Cu nor W escapes from the system during the LAL process. High-resolution O 1 s XPS spectra are shown in Fig. S3 (a–b). The peaks at 530.61, 531.13 and 532.18 eV are respectively attributed to W−O, Cu−O and H$_2$O. The special peak at 531.59 eV is associated with O−H species (H-related defects) [34]. High-resolution W 4f XPS spectrum in Fig. 2a are deconvoluated into five peaks: W^{5+} 4f$_{7/2}$ (35.00 eV), W^{6+} 4f$_{7/2}$ (35.67 eV), W^{5+} 4f$_{5/2}$ (37.07 eV), W^{6+} 4f$_{5/2}$ (37.79 eV) and W 5p$_{3/2}$ (41.34 eV). About 31.07% low-valence W^{5+} can be found. The average valence state of W can be calculated as 5.69, which is in good agreement with the Raman result. On the contrary, b-CuWO$_4$ contains no W^{5+} (Fig. S3c,). Fig. 2b shows the deconvolution of the high-resolution Cu 2p XPS spectrum of H-CuWO$_4$. Not only Cu^{2+} (935.92 eV for 2p$_{3/2}$, 955.86 eV for 2p$_{1/2}$) but also Cu^{+} (934.67 eV for 2p$_{3/2}$, 954.69 eV for 2p$_{1/2}$) can be detected. The content of low-valence Cu^{+} is about 37.21%. The other two peaks at 943.17 and 963.42 eV are the Cu^{2+} shakeup satellite peaks.

3.2. Exploration of the LAL process

Considering the above results, the product after the LAL process should be H-CuWO$_4$ nanomesh. The proposed LAL process is schematically illustrated in Fig. 2c. As shown in Fig. 2d, along c axis direction, CuWO$_4$ can be considered to be made up of alternating zigzag arrays with corner-linked [WO$_6$] and [CuO$_6$] octahedras [35]. The [WO$_6$] octahedra is nearly regular with six quasi-equilong W−O bonds. The [CuO$_6$] octahedra possesses a pseudo-tetragonally elongated geometry due to the Jahn-Teller effect of Cu^{2+}. In the LAL process, a pulsed laser beam is focused on the CuWO$_4$ powders. A plasma plume containing a mass of Cu, W and O species are produced. The resulting high temperature and pressure induce an ultrasonic adiabatic expansion of the plasma plume. Then, the plume is cooled quickly by the confining ethanol during the intermission of pulsed lasers. The species in the plume would react with the ethanol molecules. Generally, a re-crystallization process takes place. Because of the far-from thermodynamic equilibrium conditions, novel metastable structures are always

generated. As the smallest atoms in nature, H atoms are activated and accelerated to diffuse into the recrystallizing $CuWO_4$ lattice and bound to the O atoms [36]. H-interstitial $CuWO_4$ nanoparticles are therefore formed (Fig. 2e). As a result of the electron-donating behavior of H and the large electronegativity of O, electron transfer from H to O takes place [37,38]. The given electron will transfer to the central metal atom (Cu or W), resulting in the partial reduction of Cu^{2+} and W^{6+} to low-valence Cu^+ and W^{5+}. This deduction can be further demonstrated by the simultaneous partial oxidation of ethanol to ethanal (see the GC–MS spectra of the liquid before and after the LAL process in Fig. S4). The generated H-interstitial $CuWO_4$ nanoparticles are metastable with a high surface energy [39]. They would further fuse together through sharing a common crystallographic orientation among adjacent particles to minimize the high surface energy. It is the so-called oriented attachment that makes the nanoparticles self-assemble into fiber-like nanostructures [40]. Therefore, an H-$CuWO_4$ nanomesh woven by a series of fibers is produced.

According to the above discussions, we can clearly know that a reducing environment is necessary for the H intercalation step. For comparison, de-ionized water was employed as the liquid in the LAL process (200 mJ/pulse). As shown in Fig. S5, the sample is an aggregation of nanoparticles with a size similar to that of the H-$CuWO_4$ nanoparticles. Its XRD pattern in Fig. 3a corresponds to the crystalline phase of b-$CuWO_4$. The broadening of diffraction peaks is due to the reduction of crystalline size. No other peaks can be found in the pattern, indicating the absence of H intercalation. Besides, since the specific heat capacity of water (4.2) is much larger than that of ethanol (2.4), the temperature in the LAL process is decreased greatly. Self-assembly through oriented attachment into a nanomesh therefore disappears. Further, the H intercalation degree of H-$CuWO_4$ prepared in ethanol is adjustable by tuning the laser pulse energy. The corresponding product is labeled as H-$CuWO_4$-x while x represents the laser pulse energy (100, 150, 200, 250, 300 mJ/pulse). As shown in Fig. 3a, the content of $Cu_2WO_4(OH)_2$ phase increases with the increase of laser pulse energy. The appearance of $Cu_2WO_4(OH)_2$ phase should be due to the introduction of H-related defects, as demonstrated by the XRD, FTIR and XPS results. The content of $Cu_2WO_4(OH)_2$ phase therefore becomes an indicator of H intercalation degree. Meanwhile, the diffraction peaks are widened and weakened gradually because of the increase of H intercalation degree and the resulting lattice distortions.

3.3. Photocatalytic H_2 evolution evaluation

Light absorption of a semiconductor is one of the key steps determining the photo-conversion efficiency and the following

photocatalytic activity. Fig. 3b shows the absorbance spectra of b-$CuWO_4$, $CuWO_4$-200 and H-$CuWO_4$-x. Obviously, an absorption band edge can be found in each spectrum. These transitions are attributed to the ligand-to-metal charge transfer from hybridized O(2p) and Cu(3d) to W(5d) orbitals [41]. Their bandgaps can be estimated from the corresponding Tauc plots shown in Fig. S6. An indirect bandgap of 2.16 eV is obtained by b-$CuWO_4$, in agreement with the previous reports [42]. The other samples gain a larger bandgap of about 2.30 eV due to the reduced sizes and the quantum size effect. Further, the small peaks of b-$CuWO_4$ and $CuWO_4$-200 at 750 nm involve the d–d transitions in Cu^{2+} in the Jahn-Teller distorted $[CuO_6]$ octahedra [43].

As discussed above, MMCT-based polaron transfer between two neighboring nonequivalent metal atoms is an important route to broaden the light absorption range. H intercalation-induced self-doping with low-valence Cu^+ and W^{5+} takes place in H-$CuWO_4$-x. As demonstrated by the XRD results, the lattice symmetry is therefore broken, leading to a local electric field between the nonequivalent atoms. Upon the excitation of NIR irradiation, an electron is activated and transfers from the low-valence atom (Cu^+/W^{5+}) to the high-valence one (Cu^{2+}/W^{6+}) with the assistance of the local electric field [44]. Therefore, all of the H-$CuWO_4$ samples exhibit apparent NIR absorption, which is enhanced by increasing the low-valence element content.

The photocatalytic activities of the samples were evaluated upon simulated solar irradiation (AM 1.5, 100 mW cm^{-2}) in de-ionized water with ethanol as a hole scavenger. Typical time courses of H_2 evolution are shown in Fig. 4a. Neither b-$CuWO_4$ nor $CuWO_4$-200 shows photocatalytic activity. By slightly intercalating with H atoms, there is still no activity can be detected for H-$CuWO_4$-100. Interestingly, photocatalytic H_2 evolution is achieved by further increasing the H intercalation degree. The H_2 evolution rate presents a volcano-like relationship with the H intercalation degree for H-$CuWO_4$-x. A peak value of 2.79 mmol/h/g is obtained by H-$CuWO_4$-200. According to the previous reports [2,6,13,45], the photocatalytic H_2 evolution rate is generally in the order of several hundreds μmol/h/g. This peak value is much larger, indicating the favorable performance. Certainly, it can be further improved by more rational modifications.

It is known that photocatalysis generally goes hand in hand with the CB and VB potentials of the photocatalyst. The VB potentials can be determined by linear extrapolation of the leading edges of the VB XPS spectra to the base lines, shown in Fig. 4b. The CB potentials can be estimated according to the bandgaps and VB potentials. Therefore, a schematic view of the CB and VB potentials for the samples is shown in Fig. 4d. Reducing the size of $CuWO_4$ from microscale to nanoscale, CB and VB of $CuWO_4$-200 are pushed outward the center of the gap
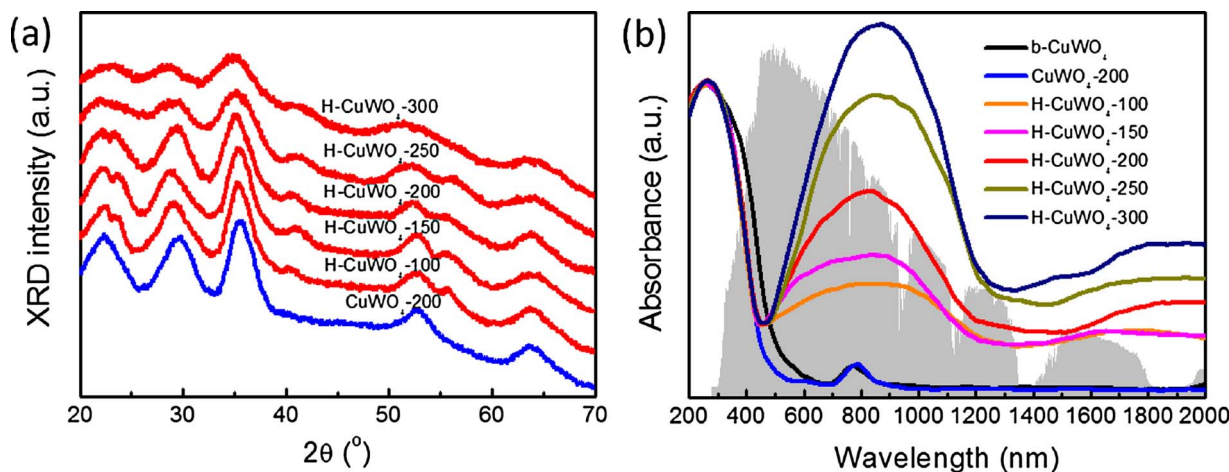

Fig. 3. (a) XRD patterns and (b) diffuse reflection absorbance spectra of the samples prepared in de-ionized water and ethanol with different laser pulse energies (100, 150, 200, 250 and 300 mJ/pulse). For comparison, solar radiation spectrum from ASTM is shown in (b).
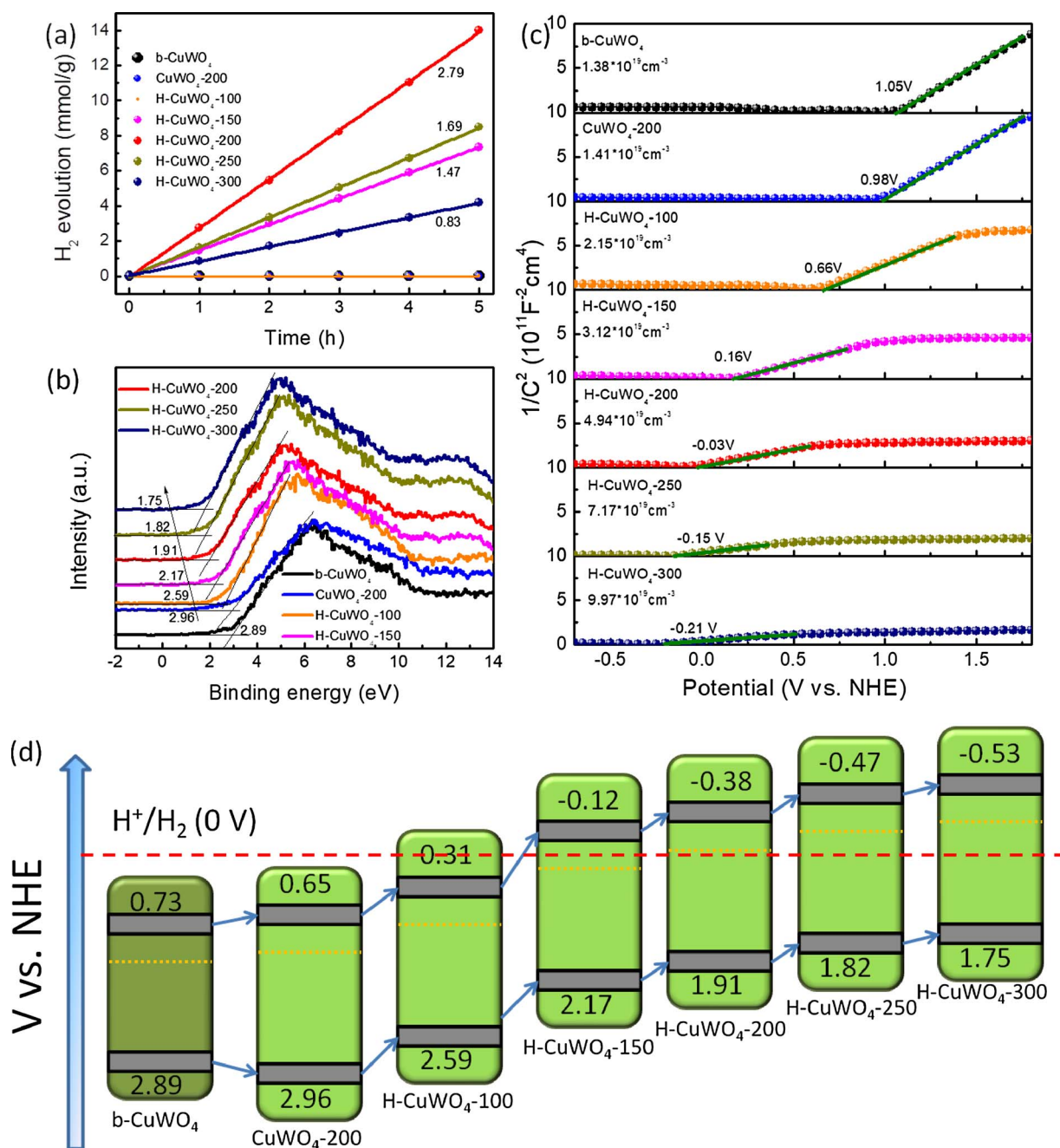
Fig. 4. (a) Typical time courses of H_2 evolution upon AM 1.5 irradiation. (b) VB XPS spectra of the samples. (c) Mott-Schottky plots of the samples. (d) A schematic view of the CB and VB potentials for the samples.

because of the quantum size effect. In agreement with the previous reports, the CB positions are located below the H^+/H_2 potential level, making b-CuWO$_4$ and CuWO$_4$-200 incapable of photocatalytic H_2 evolution. Both of CB and VB are raised up by intercalating H atoms into the lattice of nanoscaled CuWO$_4$ nanoparticles. The lifting shows a positive correlation with the H intercalation degree. The CBs of H-CuWO$_4$-x (x = 150, 200, 250 and 300) rise above the H_2 evolution potential, endowing them with favorable photocatalytic H_2 evolution activities.

To evaluate the carrier densities of the samples, Mott-Schottky measurements were conducted. All of the plots in Fig. 4c show a positive slope, suggesting that all of the samples are n-type semiconductors [46]. Flat-band potentials are determined by linear extrapolation the longest straight regions of the plots to the base lines, showing an obvious rise. Considering that CB of a n-type semiconductor

is generally about 0.3 eV above its flat-band potential [47], the CBs of the samples are also estimated to be 0.75, 0.68, 0.36, −0.14, −0.33, −0.45 and −0.51 V, respectively. This result is identical to the above analysis. Further, carrier density N_d can be calculated according to the plot slope ρ:

$$N_d = 2/(e_0 \, \varepsilon\varepsilon_0\rho) \tag{2}$$

where e_0, ε_0 and ε are respectively the electron charge, the vacuum permittivity and dielectric constant of CuWO$_4$ (8.3). It can be clearly seen that the carrier density is greatly enhanced by increasing the H intercalation degree (3.5 times for H-CuWO$_4$-200 and 7.2 times for H-CuWO$_4$-300). It is known that the electronic structures of polyxometalates are greatly influenced by their crystal structures. Both CB and VB of CuWO$_4$ are raised up because of this structure-directing effect. The intercalation of electron-donating H atoms offers H-CuWO$_4$
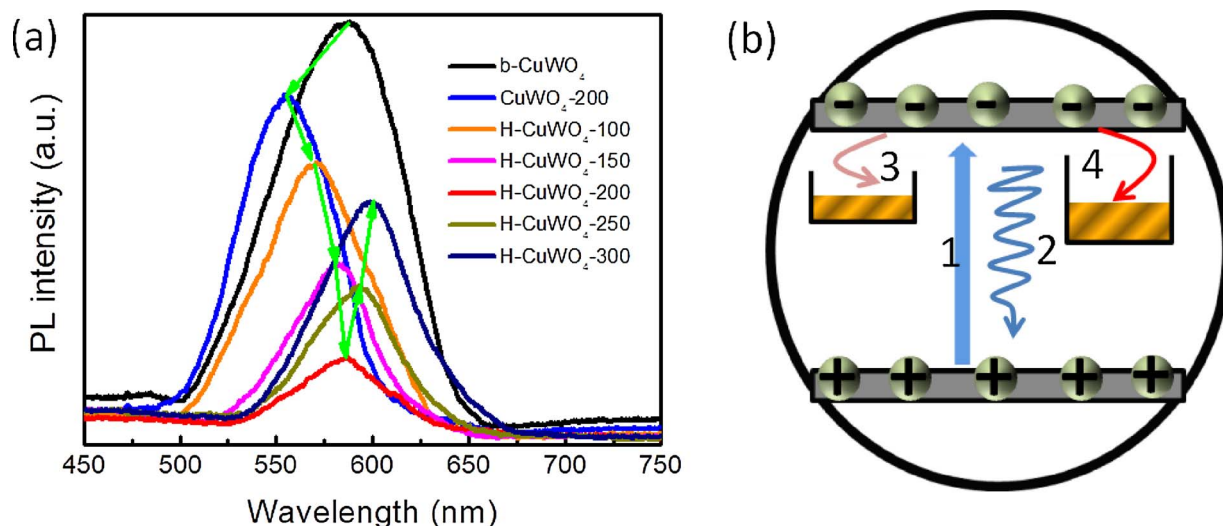
Fig. 5. (a) PL spectra of the samples. (b) Schematic illustration of the PL mechanism. (For interpretation of the references to colour in this figure legend, the reader is referred to the web version of this article.)

abundant additional electrons. The Fermi level is therefore elevated. Meanwhile, H intercalation induces a varying octahedral ligand field. The resulting stress in the lattice and the lifting of Fermi level supply the driving force for CB and VB to go upward. Similar phenomenon can be found in many previous reports. Wang et al. reported that the stress from the lattice distortion induced by the doping of Co^{2+} into TiO_2 leaded to the rising of the band structure [24]. Liao et al. prepared CoO nanoparticles for efficient water splitting, and found that surface states created abundant additional electrons for CoO and gave rise to the lifting of Fermi level, CB and VB [47]. Bloh et al. also discovered that suitable modification resulted in the stress in the ZnO lattice and the elevating of band edges [48].

From the above discussions, we can find that H-$CuWO_4$-300 performs worse than H-$CuWO_4$-200 in photocatalytic H_2 evolution although it possesses a larger carrier density and a stronger driving force for water reduction (higher CB potential). We consider that it is related to the carrier separation, the second step after carrier generation in photocatalysis. PL spectra are recorded in Fig. 5a to monitor the carrier recombination upon laser excitation with a wavelength of 325 nm (step 1 in Fig. 5b). A strong PL peak around 590 nm is gained by b-$CuWO_4$, which is attributed to the band–band PL process (step 2) [49]. $CuWO_4$-200 shows a blue-shifted band–band PL peak around 550 nm due to its broadened bandgap. The intensity is slightly weakened maybe owing to the reduced size and the weakening of bulk recombination. The strong PL quenching in H-$CuWO_4$-x indicates that the energy-wasteful carrier recombination is substantially suppressed, improving carrier separation. PL in H-$CuWO_4$ should be assigned to the excitonic PL process involving the distortion-induced sub-bands in the band gap. In this process, the excited electrons in CB are trapped by the sub-bands firstly, followed by the radiative transitions from the sub-bands to VB [50]. As a result, PL peaks are red-shifted. The red shift is increased with the increasing of H intercalation degree, suggesting that the sub-bands are moving toward the center of the gap at the same time. H intercalation firstly results in shallow sub-bands in the gap. The energy barrier around the sub-bands prevents the trapped electrons from escaping from the trapping sites to encounter with holes. Carrier recombination is therefore suppressed (step 3). However, excess H intercalation will give rise to deep sub-bands, which strongly trap the excited electrons. Carrier recombination is enhanced in spite of the energy barrier (step 4). We can clearly see that H-$CuWO_4$-200 possesses the weakest PL intensity. That would be the reason for its optimal photocatalytic performance. It will be referred to simply as H-$CuWO_4$ hereafter.

3.4. A possible dual-channel photocatalytic mechanism

The photocatalytic H_2 evolution behavior of H-$CuWO_4$ is further estimated upon various irradiations without any cocatalysts. Fig. 6a shows the time courses of H_2 evolution. Clearly, individual UV, Vis and NIR irradiations can all trigger the reactions. The H_2 evolution amounts display a quasi-linear profile with time. The H_2 evolution rates are respectively determined to be 0.38, 1.91, 0.74 mmol/h/g. It is amply demonstrated that H-$CuWO_4$ is full spectrum-active. Irradiating the H-$CuWO_4$ photocatalyst with UV and Vis together (UV&Vis), a H_2 evolution rate of 2.14 mmol/h/g is obtained. It is close to the sum of the rate values upon individual UV and Vis irradiations (UV + Vis, 2.29 mmol/h/g). As shown in Fig. 6b, the rate is further increased to 2.79 mmol/h/g by further adding NIR irradiation to form AM 1.5 solar light. It is also close to the sum of the rate values upon individual UV, Vis and NIR irradiations (UV + Vis + NIR, 3.03 mmol/h/g). The slight decrease may be due to the fact that the accumulation of photo-generated carriers will leads to carrier recombination to some extent.

In addition, when the system was kept in the dark, no H_2 can be detected. It suggests that the H_2 evolution is a photo-driven process. To further clarify the photocatalytic mechanism, single-wavelength activity of H-$CuWO_4$ in the NIR region was evaluated. As shown in Fig. 6c, H_2 evolution rate at a wavelength of 780 nm is 0.125 mmol/h/g, slightly larger than that at a wavelength of 850 nm (0.106 mmol/h/g). The decrease should be on account of the decreased light energy import of 850 nm [51]. According to Fig. 3b, H-$CuWO_4$ exhibits a larger absorbance at 850 nm. Therefore, the decrease degree of H_2 evolution rate at 850 nm is not large. The dependence of H_2 evolution rate on the light wavelength suggests that the H_2 evolution is driven by the photo-generated electrons [52].

At this point, we propose a dual-channel mechanism to describe the possible photocatalytic process (Fig. 6d). The first channel is the UV and Vis irradiations-driven H_2 evolution based on the intrinsic inter-band transition. It is discussed above that $CuWO_4$ is made up of two alternating zigzag chains with corner-linked [CuO_6] and [WO_6] octahedrals. The top of VB and the bottom of CB are mainly dominated by Cu 3d and W 5d orbitals, respectively [53]. The intrinsic inter-band transition is performed by the electron transfer from [CuO_6] to [WO_6], leaving holes in [CuO_6]. The holes are then consumed by the ethanol scavenger. At the same time, the remaining electrons are trapped by the shallow sub-bands in the gap formed by moderate H intercalation, promoting the carrier separation. The electrons are then injected into the liquid environment and drive the hydrogen reduction reactions. The other
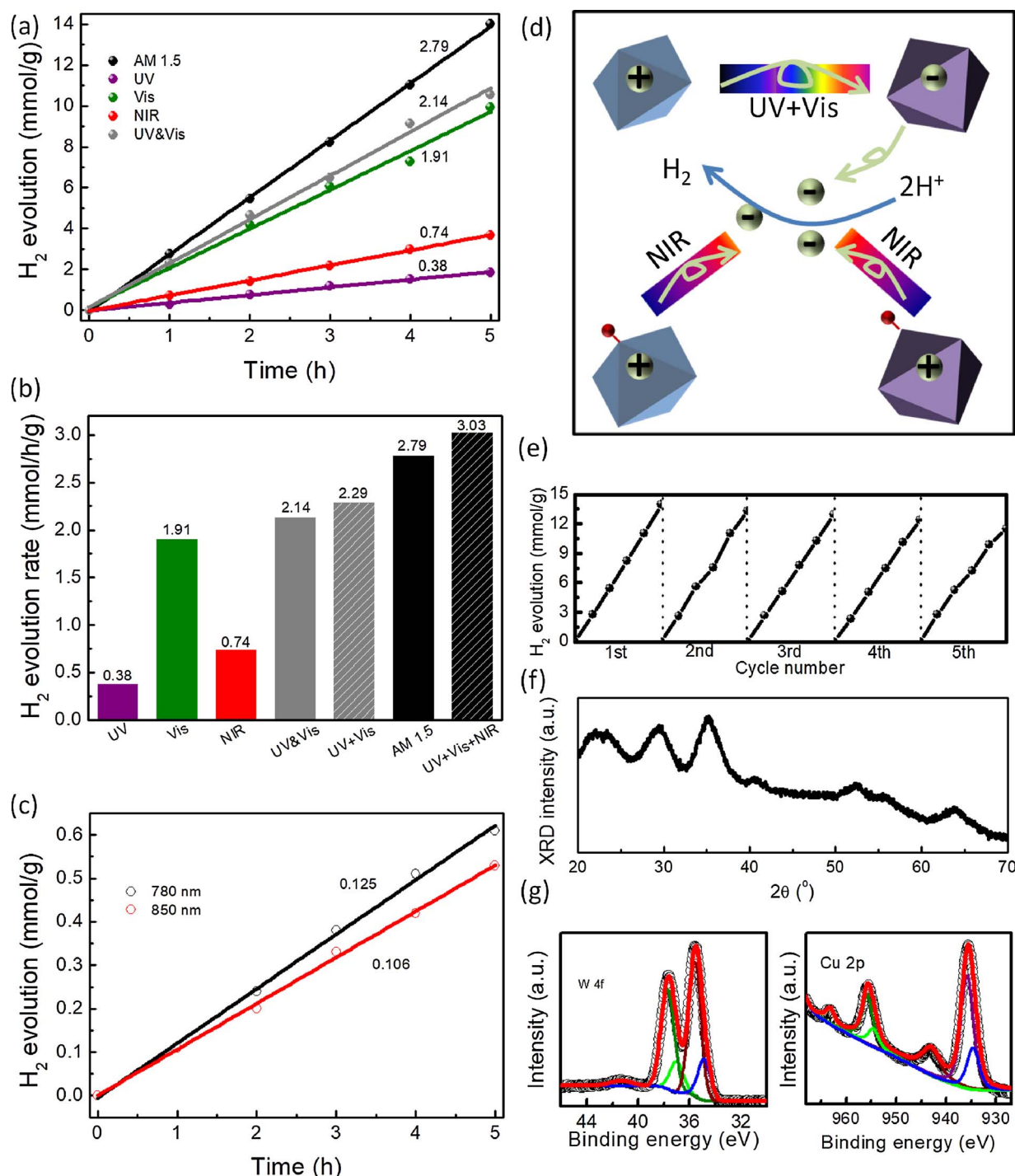
Fig. 6. (a) Typical time courses of H_2 evolution for H-CuWO$_4$ photocatalyst upon various irradiations. (b) Comparison of the H_2 evolution rates. (c) Typical time courses of H_2 evolution for H-CuWO$_4$ photocatalyst upon single-wavelength irradiations (780 and 850 nm). (d) Schematic illustration of the full spectrum-active photocatalytic process. (e) Cycling tests of H_2 evolution upon AM 1.5 irradiation. (f) XRD pattern of H-CuWO$_4$ photocatalyst after five cycles. (g) W 4f and Cu 2p XPS spectra of H-CuWO$_4$ after five cycles.

channel is the NIR light-driven H_2 evolution based on the polaron-induced MMCT. Low-valence Cu$^+$ and W^{5+} are doped into the CuWO$_4$ lattice through H intercalation. The lattice symmetry is inevitably perturbed, resulting in a local electric field between the two neighboring nonequivalent atoms. Therefore, NIR irradiation-triggered polaron absorption takes place. A free electron is then released, leaving a hole on the low-valence atom. Similarly, the holes are consumed by ethanol while the electrons reduce the H$^+$ in the solution to H_2. The mesh structure of H-CuWO$_4$ facilitates the electron transport in the photocatalytic process. Furthermore, the renewable photocatalytic

activity of H-CuWO$_4$ is investigated, shown in Fig. 6e. There is no obvious activity deterioration after five cycles, suggesting its stability. XRD pattern and XPS spectra of H-CuWO$_4$ after five cycles in Fig. 6f,g show no obvious difference between those of the fresh sample. It further demonstrates the stability of the H-CuWO$_4$ photocatalyst [54]. It is important for practical applications.

In this contribution, H-CuWO$_4$ acts as a efficient single-component photocatalyst without any cocatalysts. Generally, a cocatalyst is necessary for the photocatalytic H_2 evolution to act as an electron sink to collect electrons and promote carrier separation, and to supply active

sites for the reactions. As discussed above, the alternating zigzag chains in $CuWO_4$ make the intrinsic inter-band transition-induced electrons and holes spatially distribute in $[WO_6]$ and $[CuO_6]$ octahedrals, respectively. Further, the MMCT-induced electrons and holes are spatially separated by the local electric field between two neighboring nonequivalent atoms. The structure of $H-CuWO_4$ has already realized carrier separation. Moreover, photocatalysts with multivalent elements always display excellent photocatalytic performance since the multivalent elements can behave as the active sites. The mesh structure of $H-CuWO_4$ exposes more active sites for the H_2 evolution. Therefore, $H-CuWO_4$ can achieve H_2 evolution without the assistance of a cocatalyst [47]. Certainly, further investigation is needed to clarify the photocatalytic mechanism and improve the photocatalytic performance.

4. Conclusion

Generally, $CuWO_4$ is considered to be unable to achieve photocatalytic H_2 evolution on account of its lower CB location with respect to the H_2 evolution potential. In this work, this seemingly impossible goal has been accomplished by H intercalation into the $CuWO_4$ lattice. The H_2 evolution reactions can be driven by not only UV and Vis irradiations, but also NIR light with low single photon energy. It makes the $H-CuWO_4$ nanomesh become a single-component full spectrum-active photocatalyst for H_2 evolution. $CuWO_4$ is activated because its CB is lifted above the H_2 evolution potential by the H intercalation-induced lattice stress. A dual-channel mechanism is proposed to explain the full spectrum-active photocatalytic behavior based on two different light harvesting modes. The first one is the UV and Vis irradiations-driven intrinsic inter-band transition. The other one is the NIR light-driven MMCT. Since low-valence Cu^+ and W^{5+} are doped into the $CuWO_4$ lattice through H intercalation, the lattice symmetry is broken and a local electric filed is established. Upon NIR irradiation, polaron transfer takes place with releasing free electrons to realize hydrogen reduction. Further, the mesh structure induced by the self-assemble orientated attachment facilitates the electron transport in the photocatalytic process. Overall, we have realized full spectrum-active photocatalytic H_2 evolution in a single-component photocatalyst, which makes full use of the solar irradiation and provides new insights into the design of novel photocatalysts for practical applications.

Acknowledgements

Appendix A. Supplementary data

Supplementary data associated with this article can be found, in the online version, at https://doi.org/10.1016/j.apcatb.2018.01.021.

References

[1] A. Fujishima, K. Honda, Nature 238 (1972) 37–38.
[2] Z. Lin, L. Li, L. Yu, W. Li, G. Yang, J. Mater. Chem. A 5 (2017) 5235–5259.
[3] Y. Sang, H. Liu, A. Umar, ChemCatChem 7 (2015) 559–573.
[4] M. Zhu, X. Cai, M. Fujitsuka, J. Zhang, T. Majima, Angew. Chem. Int. Ed. 56 (2017) 1–6.
[5] L. Bai, W. Jiang, C. Gao, S. Zhong, L. Zhao, Z. Li, S. Bai, Nanoscale 8 (2016) 19014–19024.
[6] H. Yu, R. Shi, Y. Zhao, G. Waterhouse, L. Wu, C. Tung, T. Zhang, Adv. Mater. 28 (2016) 9454–9477.
[7] W. Jiang, S. Bai, L. Wang, X. Wang, L. Yang, Y. Li, D. Liu, X. Wang, Z. Li, J. Jiang, Y. Xiong, Small 12 (2016) 1640–1648.
[8] J. Wang, M. Chen, Z. Luo, L. Ma, Y. Zhang, K. Chen, L. Zhou, Q. Wang, J. Phys. Chem. C 120 (2016) 14805–14812.
[9] Y. Sang, Z. Zhao, M. Zhao, P. Hao, Y. Leng, H. Liu, Adv. Mater. 27 (2015) 363–369.
[10] Y. Yang, W. Que, X. Zhang, X. Yin, Y. Xing, M. Que, H. Zhao, Y. Du, Appl. Catal. B 200 (2017) 402–411.
[11] X. Zhang, Y. Yang, S. Ding, W. Que, Z. Zheng, Y. Du, Inorg. Chem. 56 (2017) 3386–3393.
[12] Z. Lin, J. Xiao, L. Li, P. Liu, C. Wang, G. Yang, Adv. Energy Mater. 6 (2016) 1501865.
[13] C. Gao, J. Wang, H. Xu, Y. Xiong, Chem. Soc. Rev. 46 (2017) 2799–2823.
[14] G. Li, C. Guo, M. Yan, S. Liu, Appl. Catal. B 183 (2016) 142–148.
[15] G. Wang, B. Huang, X. Ma, Z. Wang, X. Qin, X. Zhang, Y. Dai, M. Whangbo, Angew. Chem. Int. Ed. 52 (2013) 4810–4813.
[16] Z. Wu, X. Yuan, H. Wang, Z. Wu, L. Jiang, H. Wang, L. Zhang, Z. Xiao, X. Chen, G. Zeng, Appl. Catal. B 202 (2017) 104–111.
[17] M. Yan, G. Li, C. Guo, W. Guo, D. Ding, S. Zhang, Nanoscale 8 (2016) 17828–17835.
[18] D. Hu, P. Diao, D. Xu, M. Xia, Y. Gu, Q. Wu, C. Li, S. Yang, Nanoscale 8 (2016) 5892–5901.
[19] H. Chen, Y. Xu, RSC Adv. 5 (2015) 8108–8113.
[20] Z. Lin, J. Li, Z. Zheng, J. Yan, P. Liu, C. Wang, G. Yang, ACS Nano 9 (2015) 7256–7265.
[21] C. Janaky, K. Rajeshwar, N. Tacconi, W. Chanmanee, M. Huda, Catal. Today 199 (2013) 53–64.
[22] J. Xiao, P. Liu, C. Wang, G. Yang, Prog. Mater. Sci. 87 (2017) 140–220.
[23] G. Yang, Prog. Mater. Sci. 52 (2007) 648–698.
[24] T. Wang, X. Meng, G. Liu, K. Chang, P. Li, Q. Kang, L. Liu, M. Li, S. Ouyang, J. Ye, J. Mater. Chem. A 3 (2015) 9491–9501.
[25] L. Ma, J. Su, M. Liu, L. Zhang, Y. Li, L. Guo, J. Mater. Res. 31 (2016) 1616–1621.
[26] X. Zhao, W. Yao, Y. Wu, S. Zhang, H. Yang, Y. Zhu, J. Solid State Chem. 179 (2006) 2562–2570.
[27] R. Jia, Q. Wu, G. Zhang, Y. Ding, J. Mater. Sci. 42 (2007) 4887–4891.
[28] Y. Lv, W. Yao, R. Zong, Y. Zhu, Sci. Rep. 6 (2016) 19347.
[29] E. Lavrov, J. Weber, F. Borrnert, C. Walle, R. Helbig, Phy. Rev. B 66 (2002) 165205.
[30] S. Arora, M. Mathew, N. Batra, J. Cryst. Growth 88 (1988) 379–382.
[31] S. Redfern, Phy. Rev. B 48 (1993) 5761–5765.
[32] P. Siriwong, T. Thongtem, A. Phuruangrat, S. Thongtem, CrystEngComm 13 (2011) 1564–1569.
[33] J. Fuertes, D. Errandonea, A. Segura, F. Manjon, Z. Zhu, C. Tu, High Press. Res. 28 (2008) 565–570.
[34] S. Rajendran, M. Khan, F. Gracia, J. Qin, V. Gupta, S. Arumainathan, Sci. Rep. 6 (2016) 31641.
[35] L. Kihlborg, E. Gebert, Acta. Cryst. 26 (1970) 1020–1026.
[36] C. Valentin, G. Pacchioni, A. Selloni, J. Phys. Chem. C 113 (2009) 20543–20552.
[37] X. Li, J. Yu, J. Low, Y. Fang, J. Xiao, X. Chen, J. Mater. Chem. A 3 (2015) 2485–2534.
[38] Q. Wang, M. Chen, N. Zhu, X. Shi, H. Jin, Y. Zhang, Y. Cong, J. Colloid Interface Sci. 448 (2015) 407–416.
[39] H. Zhang, G. Duan, Y. Li, X. Xu, Z. Dai, W. Cai, Cryst. Growth Des. 12 (2012) 2646–2652.
[40] H. Zhang, C. Liang, Z. Tian, G. Wang, W. Cai, CrystEngComm 13 (2011) 1063–1066.
[41] T. Mavric, M. Valant, M. Forster, A. Cowan, U. Lavrencic, S. Emin, J. Colloid Interface Sci. 483 (2016) 93–101.
[42] L. Liang, H. Liu, Y. Tian, Q. Hao, C. Liu, W. Wang, X. Xie, Mater. Lett. 182 (2016) 302–304.
[43] J. Yourey, B. Bartlett, J. Mater. Chem. 21 (2011) 7651–7660.
[44] Y. Zhou, Y. Zhang, M. Lin, J. Long, Z. Zhang, H. Lin, J. Wu, X. Wang, Nat. Comm. 6 (2015) 8340.
[45] X. Li, J. Yu, J. Low, Y. Fang, J. Xiao, X. Chen, J. Mater. Chem. A 3 (2015) 2485–2534.
[46] J. Hou, H. Cheng, C. Yang, O. Takeda, H. Zhu, Nano Energy 18 (2015) 143–153.
[47] L. Liao, Q. Zhang, Z. Su, Z. Zhao, Y. Wang, Y. Li, X. Lu, D. Wei, G. Feng, Q. Yu, X. Cai, J. Zhao, Z. Ren, H. Fang, F. Robles-Hernandez, S. Baldelli, J. Bao, Nat. Nanotechnol. 9 (2014) 69–73.
[48] J.Z. Bloh, R. Dillert, D.W. Bahnemann, ChemCatChem 5 (2013) 774–778.
[49] S. Yu, B. Liu, M. Mo, J. Huang, X. Liu, Y. Qian, Adv. Funt. Mater. 13 (2003) 639–647.
[50] L. Jing, Y. Qu, B. Wang, S. Li, B. Jiang, L. Yang, W. Fu, H. Fu, J. Sun, Solar Energy Mater. Solar Cells 90 (2006) 1773–1787.
[51] P. Zhang, T. Song, T. Wang, H. Zeng, J. Mater. Chem. A 5 (2017) 22772–22781.
[52] P. Zhang, T. Song, T. Wang, H. Zeng, Appl. Catal. B 225 (2018) 172–179.
[53] P. Sarker, D. Prasher, N. Gaillard, M. Huda, J. Appl. Phys. 114 (2013) 133508.
[54] Z. Liu, Z. Yin, C. Cox, M. Bosman, X. Qian, N. Li, H. Zhao, Y. Du, J. Li, D.G. Nocera, Sci. Adv. 2 (2016) e1501425.